Ferroelastic Domain Organization and Precursor Control of Size in Solution-Grown Hafnium Dioxide Nanorods

Sean W. Depner,[†] Nicholas D. Cultrara,[†] Katie E. Farley,[†] Yueling Qin,[‡] and Sarbajit Banerjee[†,*]

[†]Department of Chemistry and [‡]Integrated Nanostructured Systems Instrumentation Facility, University at Buffalo, The State University of New York, Buffalo, New York 14260-3000, United States

ABSTRACT We demonstrate that the degree of branching of the alkyl (R) chain in a $Hf(OR)_4$ precursor allows for control over the length of HfO_2 nanocrystals grown by homocondensation of the metal alkoxide with a metal halide. An extended nonhydrolytic sol–gel synthesis has been developed that enables the growth of high aspect ratio monoclinic HfO_2 nanorods that grow along the [100] direction. The solution-grown elongated HfO_2 nanorods show remarkable organization of twin domains separated by (100) coherent twin boundaries along the length of the nanowires in a morphology reminiscent of shape memory alloys. The sequence of finely structured twin domains each spanning only a few lattice planes originates from the Martensitic transformation of the nanorods from a tetragonal to a monoclinic structure upon cooling. Such ferroelastic domain organization is uncharacteristic of metal oxides and has not thus far been observed in bulk HfO_2. The morphologies observed here suggest that, upon scaling to nanometer-sized dimensions, HfO_2 might exhibit mechanical properties entirely distinctive from the bulk.

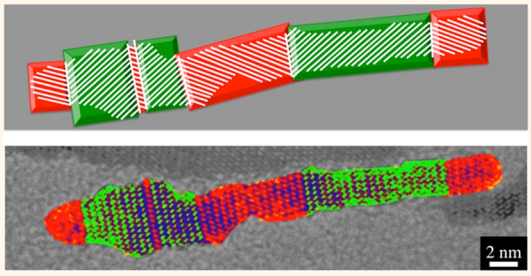

KEYWORDS: HfO_2 nanorods · ferroelasticity · twin defects · twin domain · transmission electron microscopy · Martensitic phase transformation

Scaling periodic solids to nanoscale dimensions can profoundly alter the relative phase stabilities of different polymorphs, rendering accessible metastable crystalline phases at room temperature that can otherwise only be stabilized at higher temperatures in the bulk.[1−4] The origin of the enhanced stability of a high-temperature polymorph upon scaling to finite size can be rationalized based on both thermodynamic and kinetic considerations. From a thermodynamic perspective, surface or interfacial free energy terms take on increasing prominence with decreasing particle size since a greater proportion of the constituent atoms reside in close proximity to the surface, and indeed, the surface free energy can become comparable in magnitude to the bulk free energy.[1,2,5,6] If a nanoparticle of a high-temperature polymorph crystallizes with facets characterized by an appreciably lower surface energy, it can be stabilized preferentially at room temperature with respect to the conventional stable polymorph that would otherwise be expected to be favored based on bulk free energy considerations. In addition, from the viewpoint of kinetics, phase transitions often proceed through heterogeneous (classical) nucleation and growth mechanisms wherein transitions are initiated at specific sites associated with imperfections; reduction in size exponentially decreases the probability of an imperfection occurring within a nanoparticle and thereby further favors the stabilization of metastable phases simply as a result of insurmountable activation energy barriers to nucleation[2,3] of the stable phase. The technological implications of dramatically altered phase diagrams and the stabilization of metastable phases are substantial, including enabling transformation toughening of ceramics, facilitating the design of thermochromic coatings operational at ambient temperatures, underpinning the stabilization of the twinned domain structure of shape memory alloys, and preventing the deactivation of catalysts.[1−3,5,7,8] The subtle interplay between several competing driving forces of comparable magnitude results in manifestation

* Address correspondence to sb244@buffalo.edu.

Received for review January 21, 2014 and accepted April 17, 2014.

Published online April 17, 2014
10.1021/nn501632d

TABLE 1. Calculated Surface and Bulk Energy Difference between the Monoclinic and Tetragonal Phases of HfO_2 and ZrO_2[14]

	tetragonal → monoclinic		$\Delta U_{surface,monoclinic} - \Delta U_{surface,tetragonal}$ [a]	$\Delta G_{bulk,monoclinic} - \Delta G_{bulk,tetragonal}$ [b]
oxide	transition temperature (°C)	volume expansion (%)	(mJ/m^2)	(meV)
HfO_2	1720[8,10,15,16]	2.7[19,20]	+246[14]	−196[14]
ZrO_2	1170[10,15]	∼4.0[18]	+225[14]	−140[14]

[a] Difference in surface energy between monoclinic and tetragonal phase. [b] Difference in bulk energy between monoclinic and tetragonal phase.

of intriguing physical phenomena in nanostructures that are unprecedented in the bulk. Here, we demonstrate the organization of ferroelastic domains that create a nanoscopic stripe pattern within colloidal HfO_2 nanorods. An extended nonhydrolytic sol−gel method has been developed to induce anisotropic growth of the nanorods; the quasi-periodic "bar-code"-like twin domains evidenced in these nanorods are ascribed to a Martensitic transition from an initially nucleated tetragonal phase to twin variants of a monoclinic phase[5,8−11] with the obtained self-accommodated structure being a result of dimensional confinement. The high density of twin boundaries and their organization along the length of the nanorods in a pattern reminiscent of domains in shape memory alloy materials is most unusual for nonmetallic nanostructures (particularly refractory oxides) and points to remarkable mechanical properties that can be realized in nanoscale ceramics.[12,13]

In the bulk, the monoclinic (space group $P2_1/c$) phase of HfO_2 represents the thermodynamic minimum; phase transformation to a distorted fluorite tetragonal (space group $P4_2/nmc$) phase is induced upon heating to ∼1720 °C,[8,10,15,16] and upon further heat treatment, a phase transition from the tetragonal to a cubic fluorite (space group $Fm\bar{3}m$) structure occurs at 2600 °C prior to congruent melting of the lattice at ∼2800 °C (Table 1). The symmetry-lowering tetragonal → monoclinic phase transition in HfO_2 closely parallels the better studied tetragonal → monoclinic phase transition in ZrO_2 and is believed to be Martensitic and athermal in nature.[5,8,11,16,17] In other words, the transformation is thought to proceed through a diffusionless process wherein bond distances and angles are altered without disrupting the atomic connectivity within the lattice with preservation of a mirror plane symmetry element. Such a transformation forms the basis for the celebrated transformation toughening of zirconia ceramics wherein crack propagation through metastable tetragonal grains is strongly hindered by the energy that must be expended to induce the phase transformation to the monoclinic phase.[5,18] Unlike in ZrO_2 where the phase transformation results in an almost 4% volume expansion, the tetragonal → monoclinic phase transition in HfO_2 is characterized by a more modest volume expansion estimated to be ∼2.7%.[8,19−21] Nevertheless, similar to ZrO_2, the tetragonal → monoclinic phase transformation is strongly anisotropic, being most pronounced along the *a*- and *c*-axes and negligible along the crystallographic *b*-axis. The surficial regions of grains in a bulk ceramic and the surface planes of a thin film can accommodate the volume expansion and resulting shear strain through deformation, twinning, and lattice slip mechanisms distinct from the bulk.[5,11] However, we find that in dimensionally confined nanostructures where a preponderance of the atoms are surficial, the entire free-standing nanoparticle is able to assume a distinctive morphology that has not hitherto been observed in the bulk.

Almost half a century ago, Garvie realized that below a certain critical size (variously estimated to be 15−30 nm) the tetragonal phase of ZrO_2 can be stabilized with respect to the monoclinic phase since the surface energies of the former are significantly lower than the latter.[1,6,8,22] Although the enthalpy of the tetragonal phase of ZrO_2 is more positive than that of the monoclinic phase by almost 5.4 kJ/mol, the surface energy for the former phase is 225 mJ/m^2 lower than that of the monoclinic polymorph (Table 1).[1,14,22] When the size of a particle (or an embedded crystallite in a ceramic matrix) becomes lower than the critical size, the contribution from the surface energy term more than compensates for the difference in bulk enthalpy, and the tetragonal phase is stabilized at room temperature. Much research attention has been focused on stabilizing the tetragonal phase of ZrO_2 either by scaling individual grains below the critical size or by incorporation of aliovalent (typically divalent or trivalent) cations.[5] Several synthetic approaches have also been developed in parallel for the preparation of free-standing ZrO_2 nanoparticles with hot colloidal synthetic methods being worthy of particular mention since they provide access to well-defined and monodisperse ligand-passivated nanoparticles.[9,10,15,23,24] Indeed, ZrO_2 nanoparticles grown by this method are ubiquitously stabilized in the tetragonal phase as expected from the critical size considerations outlined above.[9,10,15,23]

In contrast to ZrO_2, the critical size for stabilization of tetragonal HfO_2 is thought to be much smaller, estimated to be 4−10 nm by some authors[25] and as low as 2 nm for thin films.[20,26] Consequently, stabilization of tetragonal HfO_2 is much more difficult. Studies of bulk ceramics and thin films show numerous examples of stabilization of tetragonal ZrO_2; however, in stark contrast, monoclinic HfO_2 is stabilized upon scaling to finite size.[8,14,20] This difference has been attributed to there being a greater driving force for stabilization of

the monoclinic phase for the latter oxide since the difference in bulk free energies (ΔG) is 40% greater for HfO_2 as compared to ZrO_2 (Table 1).[8,14,20] The smaller volume expansion accompanying the tetragonal → monoclinic transformation of HfO_2 (2.7% *versus* at least 4% for ZrO_2; Table 1) also enables a facile phase transition since it implies a relatively lower resistance to transformation from the elastic strain energy expended in deforming the surrounding matrix.[8] The barrier to nucleation of the phase transition is also thought to be much lower, and conditions for nucleation of the monoclinic phase are much less stringent for HfO_2 as compared to ZrO_2.[10]

For solution-grown nanocrystals, Brus and co-workers reported stabilization of tetragonal HfO_2 upon the condensation of $HfCl_4$ and $Hf(O^iPr)_4$ at 360 °C but obtained only monoclinic nanocrystals at 400 °C.[10,15] For solid-solution $Hf_xZr_{1-x}O_2$ nanocrystals, increased Hf concentrations (high x values) appear to favor stabilization of the monoclinic phase. For solid-solution nanocrystals grown by condensation of metal alkoxides and metal halides, we have shown in past work that the degree of branching and length of the alkyl chain (R) in the $Hf(OR)_4$ or $Zr(OR)_4$ precursor provides substantial control over the stoichiometry and crystal structure of the product.[9,24] We demonstrate here that the length of HfO_2 nanorods can be tuned by choice of the precursor.

As noted above, the volume expansion that results from the Martensitic tetragonal (austenite) → monoclinic (martensite) phase transition in HfO_2 induces an anisotropic shear strain. One approach by which this transformation strain can be relieved in this symmetry-lowering transition is by formation of periodic sequences of twin variants.[2,5,10,11,17] The system seeks to establish a balance between compensating for macroscopic strain and the inevitable energetic penalty for establishing a new interface (the twin boundary).[2] In other words, by forming a sequence of periodic domains separated by a coherent twin boundary, the structural integrity of the material can be retained and the macroscopic strain can be relaxed without extensive deformation or crack propagation. McLaren and co-workers have noted both (110) and (001) twinning within the same grain for HfO_2 thin films grown on Si(100) surfaces by atomic layer deposition.[11] These authors have ascribed the observed perpendicular twinning to the need to relieve anisotropic shape strain and to ensure that grain expansion upon the phase transition from the tetragonal to the monoclinic phase is as isotropic as possible. Evidence for formation of twinned domains has also been reported in X-ray diffraction studies of polycrystalline HfO_2 samples.[17] Brus and co-workers observed twinned domains in solution-grown HfO_2 nanorods attributed to the initial stabilization of tetragonal nanocrystals that are transformed to twinned monoclinic domains upon cooling.[10] However, periodic organization of twinned domains along 1D nanorods has not thus far been evidenced in either thin films or bulk ceramic grains.

Martensitic phase transitions characterized by stabilization of periodic ferroelastic domains have applications in shape memory and superelasticity.[2,27] Indeed, the tetragonal → monoclinic phase transition has attracted recent interest owing to the intriguing observation of ferroelectric behavior in thin films of ZrO_2, $Si_xHf_{1-x}O_2$, and $Hf_xZr_{1-x}O_2$. Thin films of these materials sandwiched between TiN electrodes in a metal−insulator−metal (MIM) architecture show an appreciable ferroelectric response. Müller and co-workers have proposed that the tetragonal phase undergoes a transition to an intermediate orthorhombic (space group $Pbc2_1$) phase before transformation to the monoclinic phase to circumvent the volume expansion usually experienced by the direct tetragonal → monoclinic phase transition. The noncentrosymmetric nature of the orthorhombic phase has been invoked as the origin of the ferroelectric properties observed in these materials.[28,29] The addition of ferroelectricity to the observation of ferroelasticity demonstrated here suggests that HfO_2 may function as a multiferroic material at nanoscale dimensions.[30,31]

RESULTS AND DISCUSSION

Precursor Control of the Size of HfO_2 Nanocrystals. A modified nonhydrolytic sol−gel condensation route has been used for the growth of HfO_2 nanorods based on the condensation of hafnium alkoxides and hafnium chlorides with the elimination of alkyl halides as per[9,15,32,33]

$$\equiv Hf - X + \equiv Hf - O - R \rightarrow \equiv Hf - O - Hf \equiv + R - X \quad (1)$$

The condensation of metal halides and alkoxides to prepare metal oxides was originally developed by Vioux and later extended to the preparation of ligand-passivated TiO_2 nanocrystals by Colvin and co-workers.[34,35] Hyeon and co-workers reported the first preparation of ZrO_2 nanocrystals by this method, which was further extended to the growth of HfO_2 nanocrystals by Brus and co-workers.[15,23] In past work, we have discussed the role of the alkyl (R) group in determining the stoichiometry and phase of solid-solution $Hf_xZr_{1-x}O_2$ nanocrystals obtained by the heterocondensation of zirconium alkoxides with hafnium halides or zirconium halides with hafnium alkoxides.[9] Here, we demonstrate that the R group can be used to tune the dimensions of 1D HfO_2 nanorods in the homocondensation reaction and further report a procedure for growing high aspect ratio nanorods exhibiting a curious organized domain structure.

The nonhydrolytic sol−gel condensation reaction has been proposed to proceed through a S_N1-type mechanism with coordination of the metal halide's

metal center to the oxygen of the metal alkoxide, followed by nucleophilic attack of the alkyl group by the halide, and the elimination of the alkyl halide. It has been posited that the rate-determining step involves cleavage of the MO−R bond, and thus the electronic effects of the alkyl group and the relative stabilization of the carbocation strongly influence the kinetics of the reaction.

There is some evidence that ligand exchange as per[32,33,35]

$$MX_n + M'(OR)_n \rightarrow MX_{n-x}(OR)_x + M'X_x(OR)_{n-x} \quad (2)$$

precedes the condensation reaction and yields haloalkoxides that serve as the reactive precursors. Specifically, we have found that essentially the same stoichiometry of solid-solution $Hf_xZr_{1-x}O_2$ nanocrystals is obtained upon starting with $HfCl_4$ and $Zr(OR)_4$ as with reacting $ZrCl_4$ and $Hf(OR)_4$,[9] which supports the idea of mixed-ligand haloalkoxides being the reactive species. Furthermore, for homocondensation reactions with rare-earth cations, oxyhalides (REOCl; RE: La, Ce, Gd, Dy) or oxides can be stabilized depending upon the reaction temperature,[33,36] lending further credence to the idea of a ligand exchange step. For the growth of TiO_2, it has been suggested that $TiCl_3OPr^i$ could be a possible haloalkoxide that is generated *in situ* and could play a catalytic role in the condensation reaction.[35]

Figure 1 shows XRD patterns of HfO_2 nanocrystals synthesized by the reaction of $HfCl_4$ with different hafnium(IV) alkoxides (ethoxide, *n*-butoxide, isopropoxide, and *tert*-butoxide) for 2 h as well as for nanocrystals prepared by an extended sol−gel route with periodic injection of hafnium *tert*-butoxide over a period of 12 h. Figure 2 shows corresponding low-magnification TEM images of ensembles of nanoparticles and high-resolution transmission electron

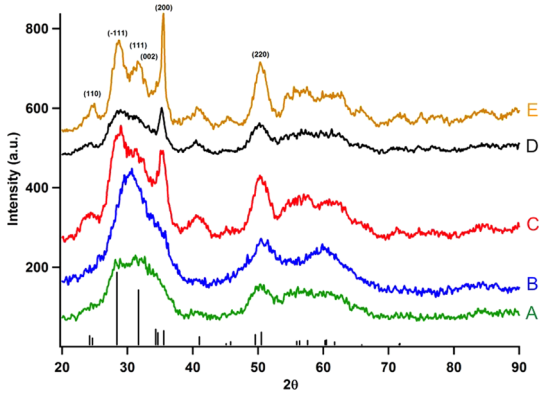

Figure 1. XRD patterns of HfO_2 nanorods synthesized by the reaction of $HfCl_4$ with the alkoxides: (A) Hf ethoxide, (B) Hf *n*-butoxide, (C) Hf isopropoxide, and (D) Hf *tert*-butoxide; each of these reactions have been performed for 2 h at 340 °C. (E) XRD pattern obtained for HfO_2 nanocrystals prepared by the reaction of $HfCl_4$ and Hf *tert*-butoxide for 12 h is also depicted. All patterns are indexed to the monoclinic phase of HfO_2 (JCPDS #78-0050).

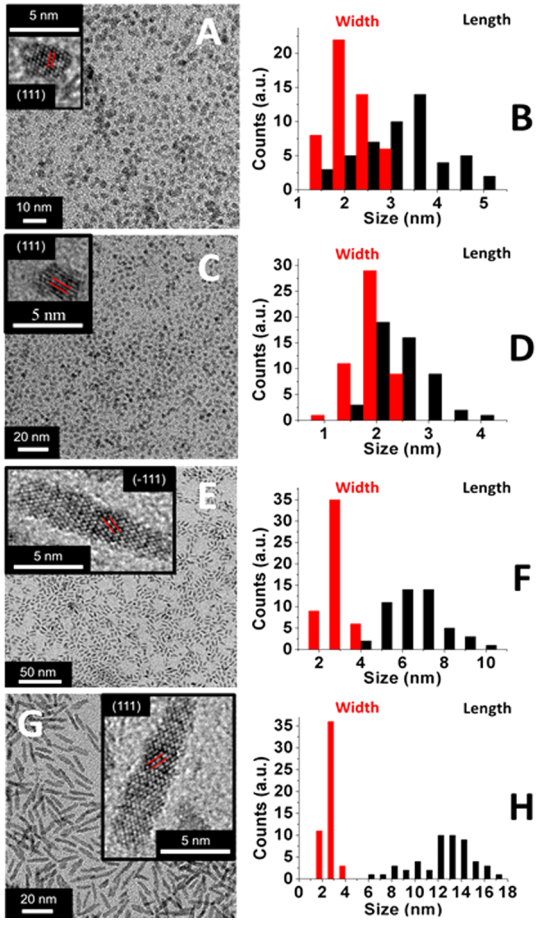

Figure 2. Low-magnification TEM images and size distribution histograms for HfO_2 nanocrystals synthesized by the reaction of $HfCl_4$ with (A,B) Hf ethoxide, (C,D) Hf *n*-butoxide, (E,F) Hf isopropoxide, and (G,H) Hf *tert*-butoxide for 2 h in each instance. The insets to A, C, E, and G indicate HRTEM images of individual nanocrystals. The separaton between lattice planes denoted by red lines is assigned to the (111) interplanar separation in each case. The inset to E depicts a nanorod with four twin defects in the crystal structure. The inset to G shows a nanorod with six discrete twin defects.

microscopy (HRTEM) images of individual HfO_2 nanoparticles from the 2 h condensation reactions along with their respective histograms indicating the distributions of width and length. While the nanocrystals obtained using ethoxide and *n*-butoxide precursors are extremely small, all of the XRD patterns are consistent with stabilization of the monoclinic (space group $P2_1/c$) phase of HfO_2 (Joint Committee on Powder Diffraction Standards (JCPDS) #78-0050). Interestingly, with increased branching of the R group, the XRD reflections become better defined, and in particular, the reflection indexed to (200) planes grows in intensity and is narrowed, suggesting (100) preferential growth planes for the nanocrystals.

The TEM images depicted in Figure 2 confirm the anisotropic growth and increase in size of the nanocrystals with increased branching of the alkyl chains of the alkoxide precursors following the sequence: ethoxide, *n*-butoxide, isopropoxide, and *tert*-butoxide.

The nanocrystals synthesized using the hafnium ethoxide and *n*-butoxide precursors are relatively isotropic, whereas those prepared using the isopropoxide and *tert*-butoxide precursors are clearly elongated. The histograms depicted in Figure 2 indicate that the average length of the HfO_2 nanorods increases from 2.7 ± 0.5 nm for nanocrystals synthesized from hafnium ethoxide to 12.9 ± 2.4 nm for those synthesized using hafnium *tert*-butoxide, whereas the width of the nanorods increases only slightly from 1.7 ± 0.3 to 2.3 ± 0.4 nm. The lattice-resolved HRTEM images depicted in the insets to Figure 2 indicate the separation between (111) planes, which are oriented at ~49.8° to the (100) planes (Figure 3). The angle to the axis of growth of the nanorod is approximately the same, suggesting that the nanorods grow along the [100] direction as also suggested by the XRD patterns in Figure 1 and observed previously for HfO_2 nanorods.[10] Figure 3 schematically depicts the preferred growth direction and the angle between the (111) and (200) planes.

The pronounced dependence of the length of the nanocrystals on the degree of branching of the alkoxide precursor is intriguing and likely arises from similar kinetic considerations as noted previously.[9] Upon initial nucleation of the nanocrystals (likely in the tetragonal phase, *vide infra*), the tertiary alkoxide stabilizes carbocation formation and facilitates S_N1 nucleophilic reactions, resulting in elimination of the alkyl halide. Accelerated kinetics for this reaction can thus lead to the more elongated nanorods for the tertiary alkoxide precursor as compared to its 1 or 2° counterparts for the same growth periods. From a nucleation perspective, an alternative explanation could be that the ethoxide precursor provides more nuclei (burst nucleation), thereby depleting the reaction mixture of monomers for HfO_2 growth. A higher nucleation density with no further addition of monomeric species (that are presumably depleted during nucleation) could stunt the growth of the nanocrystals. Notably, the reaction yield of HfO_2 nanocrystals is significantly lower for the ethoxide as compared to the *tert*-butoxide precursor, suggesting that the latter scenario is less likely since significant amounts of the unreacted precursors are recovered from this synthesis.

In an effort to further study the growth of the HfO_2 nanocrystals, an extended nonhydrolytic sol–gel method has been developed. Hafnium *tert*-butoxide has been chosen as the alkoxide precursor given the strongly elongated nanorods observed in Figure 2G and is periodically injected every 15 min over a 10 h time period. We have sought to separate nucleation and growth by first forming seed crystals and then injecting the monomer to compensate for precursors depleted by growth of the nanorods. The slow, near continuous addition of alkoxide precursors keeps the monomer concentration below supersaturation conditions where new nucleation is expected to occur. While

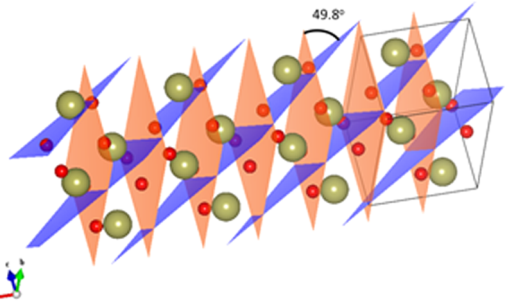

Figure 3. Crystal structure of monoclinic HfO_2 characterized by stacking of (100) growth planes. The (200) planes are depicted in orange, and the (111) plane is shown in blue; the black box delineates the unit cell.

various methods have been developed to control supersaturation,[37,38] multiple injections of small equivalents (0.5 mmol) of the alkoxide precursor yield the longest, most crystalline nanorods. Figure 4A shows a low-magnification TEM image of the HfO_2 nanorods obtained by this method, and the inset shows the size distribution histogram. The nanocrystals are on average 2.9 ± 0.5 nm in width and 31.9 ± 10.7 nm in length with some nanorods approaching lengths of ~60 nm. New nucleation appears to have been avoided for the most part, and the added precursor is instead observed to be incorporated to anisotropically grow the nanorods. Notably, the periodic addition of $HfCl_4$ does not induce the same effect, and the dimensions of the obtained nanowires are essentially unchanged from that obtained during the 2 h condensation. The resulting reaction thus has a far greater molar excess of the hafnium *tert*-butoxide precursor (total 20 mmol as compared to 2 mmol of $HfCl_4$). The continued growth of the nanorods and incorporation of Hf–O monomeric species lend credence to the idea that haloalkoxides can play a catalytic role (as observed before for $TiCl_3O$-Pr^i in the growth of TiO_2).[35] The observation that growth cannot be sustained in the presence of the halide precursor alone implies that the alkoxide is the primary source of hafnium and further underscores the importance of breaking the oxygen–carbon bond in $Hf(O-R)_4$ precursors, which is likely the origin of the pronounced dependence of the size of HfO_2 nanorods on the alkyl moiety of the alkoxide precursors.

This elongation of the nanorods is consistent with the surface-area-limited model describing anisotropic nanoparticle growth.[39] The nanorods most likely nucleate and grow as tetragonal HfO_2 nanoparticles and are transformed to the monoclinic phase upon cooling or as a result of increased crystal size above the critical threshold for the phase transformation (which is expected to be greater than the 4 nm value noted above at higher temperatures). Such a phase transformation is suggested by the stabilization of distinct twin variants formed to accommodate shear strain as observed before, illustrated in Figure 4C–E and discussed in further detail below.[10] Tetragonal HfO_2 has a stronger

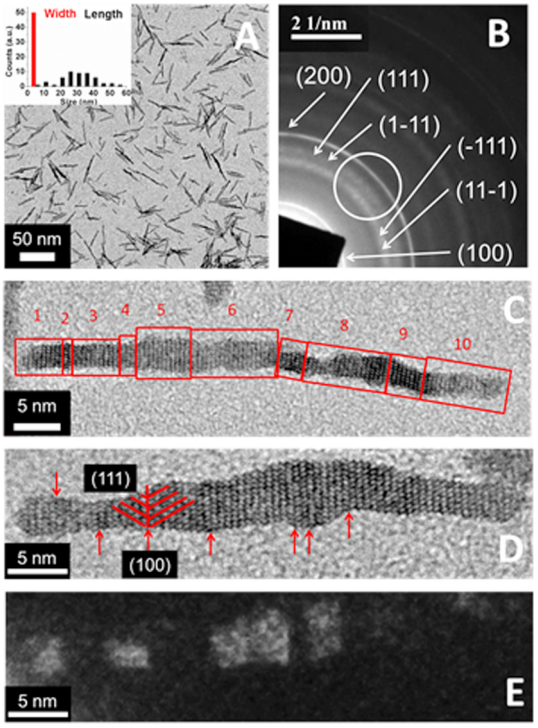

Figure 4. (A) Low-magnification TEM image of HfO_2 nanorods synthesized using the 12 h extended nonhydrolytic sol–gel method described in the text. The inset depicts a histogram showing the distribution of width and length for the nanorods. (B) Indexed selected area electron diffraction pattern illustrating diffraction spots that are selected for dark-field TEM imaging. (C) Single HfO_2 nanorod, with boxes depicting the different domains stabilized in the nanorod. (D) Lattice-resolved HRTEM image of an individual HfO_2 nanorod. Arrows indicate the (100) twin planes. Red lines highlight the (111) lattice fringes as they cross the twin plane. (E) Dark-field TEM image of D constructed using the (111) diffraction spot.

anisotropic dielectric response as compared to tetragonal ZrO_2.[40] This difference in polarization could explain why HfO_2 grows as nanorods, whereas ZrO_2 nanocrystals grown from an equivalent homocondensation reaction between $ZrCl_4$ and zirconium *tert*-butoxide are quasi-spherical. Indeed, Figure S1 (Supporting Information) shows the ZrO_2 nanocrystals obtained when $ZrCl_4$ is reacted with zirconium(IV) *tert*-butoxide for an initial period of 2 h with periodic addition of the alkoxide precursor at 15 min intervals for 10 h (the same reaction conditions as used for synthesis of HfO_2). The obtained ZrO_2 nanocrystals are ~4 nm in diameter and are crystallized in the tetragonal phase. The increased predilection of ZrO_2 to crystallize in the tetragonal phase and HfO_2 for preferring the monoclinic phase upon scaling to nanoscale dimensions has been discussed in preceding sections with respect to the smaller critical size for the latter and the relatively more modest volume expansion accompanying the phase transition.[8,10,20]

The polarization in tetragonal HfO_2 could favor stronger binding of the TOPO ligands (and/or association of Cl^- counterions) to the (001) and (010) surfaces instead of the (100) ends of the incipient nanorods (different variants are possible).[19] Such a mechanism would allow monomers to preferentially adsorb and react on the (100) facets following the diffusion-limited Lifshitz, Slyozov, and Wagner (LSW) ripening model.[39] Indeed, density functional theory calculations of monoclinic HfO_2 have indicated that, with stoichiometric termination, the ($\bar{1}$11) surface is the most stable, whereas the (100) surface is the least stable.[41] This proposed model would explain the distinctive preference for anisotropic growth observed in both XRD and HRTEM.

Ferroelastic Domain Organization in HfO_2 Nanorods. Figure 4C,D illustrates that the HfO_2 nanorods grown by the extended periodic injection sol–gel route are characterized by distinctive domains that span the diameter of the nanorods. Indeed, such domains are observed even for the "single-pot" products shown in Figure 2G,E. The lattice-resolved TEM image in Figure 4C indicates that the domains correspond to twin variants that form a sequence along the [100] direction and are organized as bands across the nanorods (see also Figures S2 and S3, Supporting Information, for other examples of highly twinned HfO_2 nanorods). Such organization of twin-related variants has been observed across >90% of the elongated HfO_2 nanorods (shorter nanorods tend to be single-domain but still monoclinic). In every instance (of ~100 particles that have been surveyed), the twin boundaries extend across the entire width of the nanorod (Figures 4 and S3). As the length of the nanorod increases, the number of twinning planes also increases, and a scatter plot depicting the number of domains *versus* aspect ratio in Figure S4 (Supporting Information) has a R^2 value of 0.77, indicating reasonable correlation between the number of twin defects and aspect ratio. Nanorods that are under 10 nm in length have at most three different domains (two coherent twin boundaries) in the same nanocrystal. As the length increases to 20 nm, 3–6 twin variants are observed in each nanocrystal. Upon increasing the length to 45 nm, as many as 10 different twin variants can be stabilized within a single HfO_2 nanorod. The twins unfailingly occur along the (100) plane; we do not observe any evidence of perpendicular twinning, multidirectional twinning, or twinning along any other crystallographic direction. The individual twins have a width of only a few lattice planes reminiscent of the behavior observed for NiTi shape memory alloys at the nanoscale[2,42] but entirely uncharacteristic of bulk HfO_2.[11,17]

Notably, the twin defects observed in the HfO_2 nanorods are very distinct from other studies that yield quasi-periodic bar-code-like patterns in anisotropic nanomaterials. For instance, periodic domains of zinc blende and wurtzite phases separated by stacking faults have been observed in II–VI semiconductor nanorods,[43] which are comparable to distinct crystal grains in a polycrystalline system and do not constitute

ferroelastic domains. The wurtzite and zinc blende phases in II−VI nanorods represent energetically proximate minima in the potential energy landscape resulting in both phases being accessible, and the stacking faults separating such domains are quite different from the twin boundaries stabilized here.

Planar defects have further been introduced within Si nanowires by using stop-flow methods during vapor−liquid−transport synthesis.[44] In this approach, the catalyst is found only on one end of the nanowire and the reaction front of the catalytic particle introduces distinctive kinks in response to switching between "stop" and "flow" conditions. When supersaturation is achieved in the catalyst particle, heterogeneous nucleation occurs initially along the most active ⟨110⟩ direction (which is not thermodynamically favorable) and then subsequently reverts to the original ⟨112⟩ growth direction. However, for HfO_2, we have not observed any evidence for growth or twinning in any direction except along the (100) planes. Indeed, Figure 2E,G as well as Figure S5 illustrates that even nanomaterials grown from single-pot reactions with no additional injection of reactants (including "nonkinked" nanorods without appreciable distortion) also show the presence of twin defects. While perturbations in growth conditions may introduce low-energy planar defects in colloidal synthesis, the scatter plot in Figure S4 (Supporting Information) suggests there is no significant difference in defect density for single-pot nanorods as compared to nanorods grown by the extended synthesis route.

Figure 4C shows a nanorod that is 54.5 nm in length and has 10 different twin variants, each separated by a (100) coherent twin boundary. The spacing between the boundaries is irregular, although the boundaries themselves always span the entire diameter of the nanorods. The domain labeled "**2**" is 1.1 nm in length, the length of two unit cells (spanning seven (111) lattice planes), whereas domain "**8**" is ∼9.9 nm in length (the length of 19 unit cells) and spans 25 lattice planes. The lattice-resolved HRTEM image in Figure 4D indicates that when the nanocrystal twins along the (100) plane, the (111) lattice planes from the two adjacent twin variants create a "V" or "Λ" shape at the (100) twin boundary, which acts like a mirror plane (highlighted by hatched lines in Figure 4D). The presence of an invariant mirror plane is characteristic of a Martensitic transformation and suggests that the array of organized twin variants is formed to accommodate the shear strain when an initially tetragonal (austenite) HfO_2 nanocrystal undergoes a phase transformation to the monoclinic (martensite) phase upon cooling (or beyond a critical size). The same nanorod shown in Figure 4D has also been examined by dark-field transmission electron microscopy (DF-TEM), as shown in Figure 4E. The nanocrystal shows a bar-code-like sequence since the (100) twin boundary separates the {111} planes into different orientations in the two variants formed on either side of the twinning plane. The two variants of the monoclinic martensite diffract to different spots along the selected area electron diffraction (SAED) pattern. The indexed SAED pattern is shown in Figure 4B. Since the pattern has been acquired for an ensemble of nanocrystals, rings are observed instead of the ideal diffraction spots expected for single-crystalline samples. The diffraction rings further have contributions from the different possible variants: (111), $(\bar{1}11)$, $(1\bar{1}1)$, and $(11\bar{1})$ planes. Consequently, the SAED pattern of monoclinic HfO_2 has been simulated from literature values of lattice parameters[45] and is shown in Figure S2B (Supporting Information). This simulation illustrates that individual sections of the diffraction pattern can be selected to image only a specific orientation of (111) planes for a single nanocrystal out of an ensemble of crystals (as seen in Figure 4E and Figure S3). An example of a typical area selected from the SAED pattern to construct the DF-TEM image is delineated by the white circle in Figure 4B. Care is taken to avoid the (100) diffraction ring as it would "brighten" the entire nanorod. The bar-code-like pattern seen in Figure 4E is exactly correspondent with the domains delineated by the observable (100) twin boundaries in Figure 4D. Figure S3 (Supporting Information) shows additional DF-TEM images indicating a similar striped pattern.

The phase transition origin of the periodic twinned domains is further corroborated by the trapping of ultrasmall nanocrystals of HfO_2 in the tetragonal phase illustrated in Figure S6. These nanocrystals are 3.1 ± 0.4 nm in size and have been stabilized by variation of the halide to active alkoxide ratio. The stabilization of the tetragonal phase at small sizes (also *via* cerium doping) suggests that the nanocrystals are initially nucleated in the tetragonal phase. With increasing particle size and upon cooling, the tetragonal phase becomes energetically less preferred for HfO_2 and a transition to the monoclinic phase likely proceeds with the stabilization of the twinned domains. The variation of the halide/alkoxide ratio allows for a means to slow the kinetics of the condensation reaction allowing for stabilization of the ultrasmall nanocrystals and will be explored in future work.

The striped bar-code-like organization of twin variants in the HfO_2 nanorods is most unusual for binary oxides or, for that matter, nonmetallic materials. Unlike in bulk HfO_2, wherein surficial and interior regions separately accommodate the shear strain and volume expansion arising from the tetragonal → monoclinic phase transition through microcracks, surface uplifts, deformations, and perpendicular twinning,[5,8,11,17] the entire nanocrystal "self-accommodates" strain here through periodic organization of twin boundaries. As summarized in Table 1, the driving force for the Martensitic transformation of tetragonal HfO_2 is much greater than for ZrO_2 (as further evidenced by the stabilization of tetragonal ZrO_2 upon performing an equivalent homocondensation reaction (Figure S1)).

The change in total free energy ($\Delta G_{t\rightarrow m}$) upon cooling initially tetragonal nanorods to the monoclinic phase can be expressed as[5]

$$\Delta G_{t\rightarrow m} = \Delta G_{bulk} + \Delta U_{matrix} + \Delta U_{surface} + \Delta U_{interfaces} \quad (3)$$

where ΔG_{bulk} is the difference in chemical free energy between the two phases (Table 1 indicates a value of −196 meV predicted by DFT calculations). At room temperature, this value is strongly negative and is the major driving force for the transition given that the monoclinic phase is the thermodynamically favored phase in the bulk. ΔU_{matrix} corresponds to the elastic strain energy expended during the transition and is dependent on the external matrix. Notably, even in free-standing nanocrystals, the deformation of the ligand shell that must accompany the phase transition is not negligible.[46] ΔU_{matrix} is >0 since strain energy must be expended to deform the matrix around the nanoparticles, and this term essentially counteracts the chemical potential driving force for the transition. $\Delta U_{surface}$ (which has also been predicted and experimentally verified to be a positive quantity)[14,20,41] corresponds to the change in surface energy upon phase transformation of the nanocrystals.[1]

$$\Delta U_{surface} = \gamma_m S_m - \gamma_t S_t \quad (4)$$

where γ_m and γ_t are free energy per unit surface area for the monoclinic and tetragonal phases, respectively, and S_m and S_t are the surface areas of the monoclinic and tetragonal phase, respectively. Finally, $\Delta U_{interfaces}$ is the energy expended to create new interfaces such as the coherent twin boundaries observed in Figures 4 and S2. In bulk HfO_2, the ΔU_{matrix} and the ($\Delta U_{surface}$ + $\Delta U_{interfaces}$) contributions vary greatly within the interior of a sample and on the surface, and thus the driving force for the transition is different within the two regions. In stark contrast, the entire crystal adopts the striped morphology upon scaling to nanometer-sized dimensions.

In the HfO_2 nanorods, the ΔG_{bulk} driving force that induces the tetragonal → monoclinic phase transformation is primarily counteracted by the energy expended to deform the ligand shell (ΔU_{matrix}), the increase in the surface energy ($\Delta U_{surface}$), and the creation of new interfaces ($\Delta U_{interfaces}$).[5] The narrow width of the nanorods likely facilitates the creation of twin boundaries as an alternative to other deformations (note that small bumps are also observed in Figure 4, which could also represent another route to accommodating the transformational strain and volume expansion resulting from the phase transformation). Given the small surface area of the twin interfaces (the nanorods have a diameter of only 2.9 ± 0.5 nm as depicted in the inset Figure 4A), the twin boundary energies are likely low, allowing for the finely structured

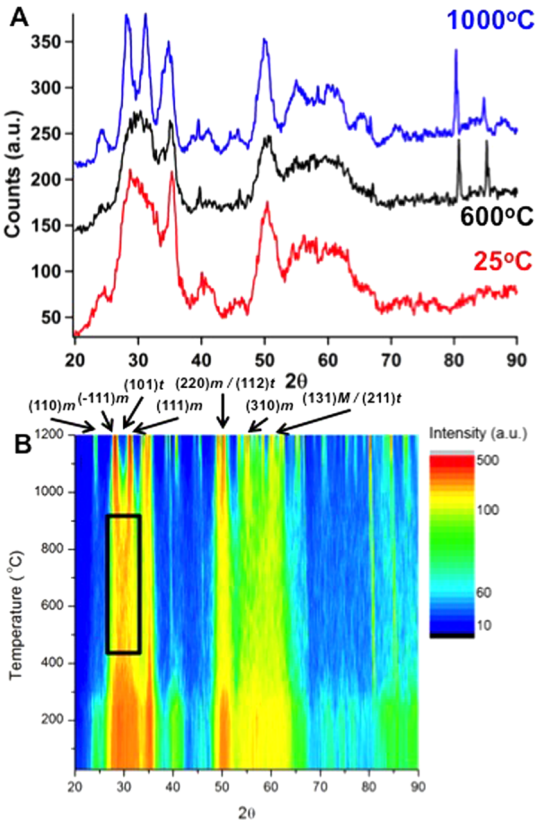

Figure 5. Temperature-dependent XRD profiles of HfO_2 nanocrystals (grown by reaction of $HfCl_4$ with Hf(IV) *tert*-butoxide). (A) XRD patterns acquired at room temperature, 600 °C, and 1000 °C and (B) contour plot of the XRD patterns collected between room temperature and 1200 °C. The area highlighted by the box shows the emergence of (101) reflections of tetragonal HfO_2 prior to domination of the monoclinic phase as the nanocrystals are sintered.

sequence of twin variants spanning only a few lattice planes in length.[2,42] The energetic penalty involved in creating the twin boundaries must then be offset by compensation of the transformation strain across the different variants, allowing for the structural integrity of the nanorods to be maintained.[2] Indeed, calculations examining the balance between the interfacial energy at twin boundaries and the elastic strain energy for spatially confined materials undergoing an austenite → martensite phase transformation have indicated that, with increasing dimensional confinement, the sequence of twin variants becomes more finely structured.[47,48] Such behavior is observed for the first time here for an oxide material. Martensitic materials exhibiting a symmetry-lowering phase transformation and domain structuring are ferroelastic, and the observations here suggest the potential manifestation of shape memory behavior in ultrathin HfO_2 nanowires.[2,7,27]

Figure 5 shows temperature-dependent XRD profiles acquired for 12.9 ± 2.4 nm long HfO_2 nanocrystals grown by reacting 2 mmol $HfCl_4$ with 2 mmol Hf(IV) *tert*-butoxide. The contour plot shows the emergence of $(101)_{tetragonal}$ reflections (between the $(\bar{1}11)$ and

(111) monoclinic reflections) around 400 °C, and a mixture of tetragonal and monoclinic polymorphs is maintained until ~800 °C at which point the nanocrystals begin to sinter into larger particles. Larger particles have a much stronger preference for the monoclinic phase as per the arguments regarding the critical threshold size articulated above. Consequently, with sintering, the nanocrystals are transformed to the monoclinic phase and remain in this structure up until the 1200 °C limit of our capabilities. In other words, while the emergence of the tetragonal phase is observed, sintering (this competition between phase transformation and sintering has also been observed by Brus and co-workers)[10] precludes stabilization of phase-pure tetragonal HfO_2 upon annealing of monoclinic nanocrystals. Additionally, the introduction of twin defects is also known to further increase the hysteresis for diffusionless transitions.[16]

CONCLUSIONS

In conclusion, elongated HfO_2 nanorods are believed to nucleate in the tetragonal phase and are transformed to the monoclinic phase upon cooling. The nanocrystals may also undergo the tetragonal → monoclinic phase transformation as a result of growth past the critical size at elevated temperatures. The alkyl (R) group of the $Hf(OR)_4$ precursor used in the homocondensation reaction is found to profoundly affect the length of the nanorods (grown along the [100] direction) in the order: *tert*-butoxide > isopropoxide > *n*-butoxide > ethoxide. The rate of the homocondensation reaction is thought to be accelerated with increased branching of the alkyl groups due to a rate-determining step involving cleavage of the O−R bonds in $Hf(OR)_4$. A synthetic route has been devised to grow elongated nanorods approaching ~60 nm in length (still only ~2.9 nm in diameter) based on multiple injections of small equivalents of the hafnium *tert*-butoxide precursor.

The elongated HfO_2 nanorods are characterized by a remarkable striped bar-code-like pattern of twin variants separated by (100) coherent twin boundaries and organized along the length of the nanorods, reminiscent of ferroelastic domains observed in shape memory materials. The twin variants are formed to accommodate the transformation strain accompanying the symmetry-lowering Martensitic transformation of the nanorods from the tetragonal to the monoclinic phase. The strong dimensional confinement of the nanowires implies low twin interface energies for twins that span the entire diameter of the nanorods and allows for compensation of the shear strain by stabilization of very finely structured twin variants that span only a few lattice planes. The ferroelastic behavior and organization of the twin domains is most readily apparent in DF-TEM images. Future work will focus on the study of domain wall movement and plastic deformation under applied stress in individual nanorods to examine the potential manifestation of shape memory effects.

METHODS

$HfCl_4$ (99.9% purity), $ZrCl_4$ (99.95% purity), hafnium isopropoxide, zirconium *tert*-butoxide, and tri-*n*-octylphosphine oxide (TOPO) (90% purity) were purchased from Strem. Hafnium ethoxide and hafnium *n*-butoxide were purchased from Gelest. Hafnium *tert*-butoxide was purchased from Alfa-Aesar. All chemicals were used as received. In a typical synthesis, 2 mmol of $HfCl_4$ and 2 mmol of hafnium(IV) alkoxide $Hf(OR)_4$ (R: et, ^{i}Pr, *n*-but, or *tert*-but) are weighed out in a glovebox under an Ar atmosphere and placed in a reaction vessel containing 10 g of TOPO. The reaction mixture is then heated on a Schlenk line under an argon atmosphere at a temperature of 340 °C for 2 h. At the end of the reaction, the reaction flask is cooled to ~60 °C and the nanoparticles are flocculated by the addition of an excess of acetone. The flocculated nanocrystals are removed from solution by centrifugation at 12 000 rpm. Next, the precipitate is dissolved in hexane and centrifuged at 1500 rpm. Several washing/reprecipitation cycles are then performed alternately using hexane and acetone, followed by centrifugation.

An extended nonhydrolytic sol−gel synthetic route has been developed to increase the length of the HfO_2 nanorods. Seed nanocrystals are first synthesized from the condensation reaction between 2 mmol $HfCl_4$ and 2 mmol of hafnium *tert*-butoxide, as described above. However, at the end of the 2 h reaction time, an additional 0.5 mmol of hafnium *tert*-butoxide is added to the reaction vessel every 15 min for 10 h. The additional alkoxide precursor is weighed out under an Ar atmosphere in a glovebox and stored in a separate three-neck flask under an Ar ambient at room temperature on the same Schlenk line. The 0.5 mmol equivalents are transferred to the primary reaction vessel using a syringe at 15 min intervals. Subsequently, the reaction mixture is cooled to ~60 °C, and the nanocrystals are recovered and purified as previously stated by addition of acetone and centrifugation.

X-ray diffraction (XRD) was performed using a Rigaku Ultima IV diffractometer using graphite-monochromated Cu Kα radiation (λ = 0.15418 nm) with an accelerating voltage of 40 kV and 44 mA current in the 2θ range from 20 to 90° at a scanning rate of 2° min^{-1}. *In situ* heating during XRD was performed on a Rigaku Ultima IV diffractometer at a scanning rate of 1° min^{-1} in the 2θ range between 20 and 90° with a sampling width of 0.05 2θ using graphite-monochromated Cu Kα radiation. *In situ* heating was performed using an Ultima IV HT 1500 temperature attachment with a PTC-30 programmable temperature controller and a platinum sample holder. Heating was performed at a rate of 10 °C/min with a temperature hold time of 30 min prior to acquiring each pattern.

A JEOL-2010 electron microscope, operated at 200 kV, was used for HRTEM, DF-TEM, bright-field transmission electron microscopy and for acquiring SAED patterns.

Conflict of Interest: The authors declare no competing financial interest.

Acknowledgment. We gratefully acknowledge support from the National Science Foundation under DMR 0847169.

Supporting Information Available: Figures showing data for ZrO_2 nanocrystals prepared *via* the 12 h extended nonhydrolytic sol−gel synthesis, simulation for HfO_2 diffraction patterns, additional DF-TEM images, analysis of number of defects *versus* aspect ratio, and additional TEM images of HfO_2 nanocrystals. This material is available free of charge *via* the Internet at http://pubs.acs.org.

REFERENCES AND NOTES

1. Navrotsky, A. Nanoscale Effects on Thermodynamics and Phase Equilibria in Oxide Systems. *ChemPhysChem* **2011**, *95616*, 2207–2215.
2. Waitz, T.; Tsuchiya, K.; Antretter, T.; Fischer, F. D. Phase Transformations of Nanocrystalline Martensitic Materials. *MRS Bull.* **2009**, *34*, 814–821.
3. Whittaker, L.; Patridge, C. J.; Banerjee, S. Microscopic and Nanoscale Perspective of the Metal−Insulator Phase Transitions of VO_2: Some New Twists to an Old Tale. *J. Phys. Chem. Lett.* **2011**, *2*, 745–758.
4. Tian, P.; Zhang, Y.; Senevirathne, K.; Brock, S. L.; Dixit, A.; Lawes, G.; Billinge, S. J. L. Diverse Structural and Magnetic Properties of Differently Prepared MnAs Nanoparticles. *ACS Nano* **2011**, *5*, 2970–2978.
5. Chevalier, J.; Gremillard, L.; Virkar, A. V.; Clarke, D. R. The Tetragonal-Monoclinic Transformation in Zirconia: Lessons Learned and Future Trends. *J. Am. Ceram. Soc.* **2009**, *92*, 1901–1920.
6. Garvie, R. C. The Occurrence of Metastable Tetragonal Zirconia as a Crystallite Size Effect. *J. Phys. Chem.* **1965**, *69*, 1238–1243.
7. Van Humbeeck, J. Shape Memory Alloys: A Material and a Technology. *Adv. Eng. Mater.* **2001**, *3*, 837–850.
8. Wang, J.; Li, H. P.; Stevens, R. Hafnia and Hafnia-Toughened Ceramics. *J. Mater. Sci.* **1992**, *27*, 5397–5430.
9. Depner, S. W.; Kort, K. R.; Banerjee, S. Precursor Control of Crystal Structure and Stoichiometry in Twin Metal Oxide Nanocrystals. *CrystEngComm* **2009**, *11*, 841–846.
10. Tang, J.; Zhang, F.; Zoogman, P.; Fabbri, J.; Chan, S. W.; Zhu, Y.; Brus, L. E.; Steigerwald, M. L. Martensitic Phase Transformation of Isolated HfO_2, ZrO_2, and $Hf_xZr_{1-x}O_2$ ($0 < x < 1$) Nanocrystals. *Adv. Funct. Mater.* **2005**, *15*, 1595–1602.
11. MacLaren, I.; Ras, T.; MacKenzie, M.; Craven, A. J.; McComb, D. W.; De Gendt, S. Texture, Twinning, and Metastable "Tetragonal" Phase in Ultrathin Films of HfO_2 on a Si Substrate. *J. Electrochem. Soc.* **2009**, *156*, G103.
12. Zhang, H.; Ha, D. H.; Hovden, R.; Kourkoutis, L. F.; Robinson, R. D. Controlled Synthesis of Uniform Cobalt Phosphide Hyperbranched Nanocrystals Using Tri-*n*-Octylphosphine Oxide as a Phosphorus Source. *Nano Lett.* **2011**, *11*, 188–197.
13. Xia, Y.; Xiong, Y.; Lim, B.; Skrabalak, S. E. Shape-Controlled Synthesis of Metal Nanocrystals: Simple Chemistry Meets Complex Physics? *Angew. Chem., Int. Ed.* **2009**, *48*, 60–103.
14. Iskandarova, I. M.; Knizhnik, A. A.; Rykova, E. A.; Bagatur'yants, A. A.; Potapkin, B. V.; Korkin, A. A. First-Principle Investigation of the Hydroxylation of Zirconia and Hafnia Surfaces. *Microelectron. Eng.* **2003**, *69*, 587–593.
15. Tang, J.; Fabbri, J.; Robinson, R. D.; Zhu, Y.; Herman, I. P.; Steigerwald, M. L.; Brus, L. E. Solid-Solution Nanoparticles: Use of a Nonhydrolytic Sol−Gel Synthesis To Prepare HfO_2 and $Hf_xZr_{1-x}O_2$ Nanocrystals. *Chem. Mater.* **2004**, *16*, 1336–1342.
16. Wolten, G. M. Diffusionless Phase Transformations in Zirconia and Hafnia. *J. Am. Ceram. Soc.* **1963**, *46*, 418–422.
17. Gasdaska, C. J.; Whalen, P. J.; Marti, J.; Reidinger, F. Texture and Recrystallization on Ground Surfaces of Hafnia. *J. Am. Ceram. Soc.* **1990**, *73*, 1941–1946.
18. Garvie, R. C.; Hannink, R. H.; Pascoe, R. T. Ceramic Steel? *Nature* **1975**, *258*, 703–704.
19. Trolliard, G.; Mercurio, D.; Perez-Mato, J. M. Martensitic Phase Transition in Pure Zirconia: A Crystal Chemistry Viewpoint. *Z. Kristallogr.* **2011**, *226*, 264–290.
20. Zhou, W.; Ushakov, S. V.; Wang, T.; Ekerdt, J. G.; Demkov, A. A.; Navrotsky, A. Hafnia: Energetics of Thin Films and Nanoparticles. *J. Appl. Phys.* **2010**, *107*, 123514.
21. Stacy, D. W.; Johnstone, J. K.; Wilder, D. R. Axial Thermal Expansion of HfO_2. *J. Am. Ceram. Soc.* **1972**, *55*, 482–483.
22. Pitcher, M. W.; Ushakov, S. V.; Navrotsky, A.; Woodfield, B. F.; Li, G.; Boerio-Goates, J.; Tissue, B. M. Energy Crossovers in Nanocrystalline Zirconia. *J. Am. Ceram. Soc.* **2005**, *88*, 160–167.
23. Joo, J.; Yu, T.; Kim, Y. W.; Park, H. M.; Wu, F.; Zhang, J. Z.; Hyeon, T. Multigram Scale Synthesis and Characterization of Monodisperse Tetragonal Zirconia Nanocrystals. *J. Am. Chem. Soc.* **2003**, *125*, 6553–6557.
24. Navarro, D. A.; Depner, S. W.; Watson, D. F.; Aga, D. S.; Banerjee, S. Partitioning Behavior and Stabilization of Hydrophobically Coated HfO_2, ZrO_2 and $Hf_xZr_{1-x}O_2$ Nanoparticles with Natural Organic Matter Reveal Differences Dependent on Crystal Structure. *J. Hazard. Mater.* **2011**, *196*, 302–310.
25. Hunter, O., Jr.; Scheidecker, R. W.; Togo, S. Characterization of Metastable Tetragonal Hafnia. *Ceramurgia Int.* **1979**, *5*, 137–142.
26. Ushakov, S. V.; Navrotsky, A.; Yang, Y.; Stemmer, S.; Kukli, K.; Ritala, M.; Leskelä, M. A.; Fejes, P.; Demkov, A.; Wang, C.; *et al.* Crystallization in Hafnia- and Zirconia-Based Systems. *Phys. Status Solidi B* **2004**, *241*, 2268–2278.
27. Ren, X.; Wang, Y.; Otsuka, K.; Lloveras, P. Ferroelastic Nanostructures and Nanoscale Transitions: Ferroics with Point Defects. *MRS Bull.* **2009**, *34*, 838–846.
28. Müller, J.; Böscke, T. S.; Schröder, U.; Mueller, S.; Bräuhaus, D.; Böttger, U.; Frey, L.; Mikolajick, T. Ferroelectricity in Simple Binary ZrO_2 and HfO_2. *Nano Lett.* **2012**, *12*, 4318–4323.
29. Böscke, T. S.; Müller, J.; Bräuhaus, D.; Schröder, U.; Böttger, U. Ferroelectricity in Hafnium Oxide Thin Films. *Appl. Phys. Lett.* **2011**, *99*, 102903.
30. Zheng, H.; Wang, J.; Lofland, S. E.; Ma, Z.; Mohaddes-Ardabili, L.; Zhao, T.; Salamanca-Riba, L.; Shinde, S. R.; Ogale, S. B.; Bai, F.; *et al.* Multiferroic $BaTiO_3$-$CoFe_2O_4$ Nanostructures. *Science* **2004**, *303*, 661–663.
31. Chu, Y. H.; Martin, L. W.; Holcomb, M. B.; Gajek, M.; Han, S. J.; He, Q.; Balke, N.; Yang, C. H.; Lee, D.; Hu, W.; *et al.* Electric-Field Control of Local Ferromagnetism Using a Magnetoelectric Multiferroic. *Nat. Mater.* **2008**, *7*, 478–482.
32. Depner, S. W.; Kort, K. R.; Jaye, C.; Fischer, D. A.; Banerjee, S. Nonhydrolytic Synthesis and Electronic Structure of Ligand-Capped $CeO_{2-\delta}$ and CeOCl Nanocrystals. *J. Phys. Chem. C* **2009**, *113*, 14126–14134.
33. Kort, K. R.; Banerjee, S. Shape-Controlled Synthesis of Well-Defined Matlockite LnOCl (Ln: La, Ce, Gd, Dy) Nanocrystals by a Novel Non-hydrolytic Approach. *Inorg. Chem.* **2011**, *50*, 5539–5544.
34. Trentler, T. J.; Denler, T. E.; Bertone, J. F.; Agrawal, A.; Colvin, V. L. Synthesis of TiO_2 Nanocrystals by Nonhydrolytic Solution-Based Reactions. *J. Am. Chem. Soc.* **1999**, *121*, 1613–1614.
35. Vioux, A. Nonhydrolytic Sol−Gel Routes to Oxides. *Chem. Mater.* **1997**, *9*, 2292–2299.
36. Kort, K. R.; Banerjee, S. Oriented Electrophoretic Deposition of GdOCl Nanoplatelets. *J. Phys. Chem. B* **2013**, *117*, 1585–1591.
37. Jin, S.; Bierman, M. J.; Morin, S. A. A New Twist on Nanowire Formation: Screw-Dislocation-Driven Growth of Nanowires and Nanotubes. *J. Phys. Chem. Lett.* **2010**, *1*, 1472–1480.
38. Dagtepe, P.; Chikan, V. Quantized Ostwald Ripening of Colloidal Nanoparticles. *J. Phys. Chem. C* **2010**, *114*, 16263–16269.
39. Seyed-Razavi, A.; Snook, I. K.; Barnard, A. S. Surface Area Limited Model for Predicting Anisotropic Coarsening of Faceted Nanoparticles. *Cryst. Growth Des.* **2011**, *11*, 158–165.
40. Zhao, X.; Vanderbilt, D. First-Principles Study of Structural, Vibrational, and Lattice Dielectric Properties of Hafnium Oxide. *Phys. Rev. B* **2002**, *65*, 233106.
41. Luo, X.; Demkov, A.; Triyoso, D.; Fejes, P.; Gregory, R.; Zollner, S. Combined Experimental and Theoretical Study of Thin Hafnia Films. *Phys. Rev. B* **2008**, *78*, 245314.
42. Waitz, T.; Spišák, D.; Hafner, J.; Karnthaler, H. P. Size-Dependent Martensitic Transformation Path Causing Atomic-Scale Twinning of Nanocrystalline NiTi Shape Memory Alloys. *Europhys. Lett.* **2005**, *71*, 98–103.
43. Hughes, S. M.; Alivisatos, A. P. Anisotropic Formation and Distribution of Stacking Faults in II−VI Semiconductor Nanorods. *Nano Lett.* **2013**, *13*, 106–110.
44. Tian, B.; Xie, P.; Kempa, T. J.; Bell, D. C.; Lieber, C. M. Single-Crystalline Kinked Semiconductor Nanowire Superstructures. *Nat. Nanotechnol.* **2009**, *4*, 824–829.

45. Lowther, J.; Dewhurst, J.; Leger, J.; Haines, J. Relative Stability of ZrO_2 and HfO_2 Structural Phases. *Phys. Rev. B* **1999**, *60*, 14485–14488.
46. Banerjee, S.; Jia, S.; Kim, D. I.; Robinson, R. D.; Kysar, J. W.; Bevk, J.; Herman, I. P. Raman Microprobe Analysis of Elastic Strain and Fracture in Electrophoretically Deposited CdSe Nanocrystal Films. *Nano Lett.* **2006**, *6*, 175–180.
47. Hackl, K.; Schmidt-Baldassari, M.; Zhang, W.; Eggeler, G. Surface Energies and Size-Effects in Shape-Memory-Alloys. *Mater. Sci. Eng., A* **2004**, *378*, 499–502.
48. Waitz, T.; Antretter, T.; Fischer, F. D.; Simha, N. K.; Karnthaler, H. P. Size Effects on the Martensitic Phase Transformation of NiTi Nanograins. *J. Mech. Phys. Solids* **2007**, *55*, 419–444.